Generation and life cycle of the dipole in the South China Sea summer circulation

Guihua Wang,[1] Dake Chen,[2,1] and Jilan Su[1]

Received 25 September 2005; revised 13 February 2006; accepted 3 March 2006; published 1 June 2006.

[1] The South China Sea (SCS) summer circulation often has a dipole structure associated with an eastward jet, appearing off central Vietnam. The dipole has an anticyclonic eddy (AE) south of the jet and a cyclonic eddy (CE) north of it. The life cycle of the dipole structure is analyzed using satellite altimetry data and a reduced gravity model. On average the dipole structure begins in June, peaks in strength in August or September, and disappears in October. The dipole evolution lags behind the basin scale wind by about 40 days, and 40 days are exactly what it takes for baroclinic planetary waves to cross the southern SCS. Our results show that the vorticity transports from the nonlinear effect of the western boundary currents are crucial for the generation of the dipole structure. In addition, the strength and direction of the offshore wind jet also play a significant role in determining the magnitudes and the core positions of the two concomitant eddies.

Citation: Wang, G., D. Chen, and J. Su (2006), Generation and life cycle of the dipole in the South China Sea summer circulation, *J. Geophys. Res.*, *111*, C06002, doi:10.1029/2005JC003314.

1. Introduction

[2] The South China Sea is the largest semi-enclosed marginal sea in the western tropic Pacific (Figure 1). Its upper layer circulation is driven mainly by the monsoon, with additional influence from the Kuroshio in its northern part [*Qu*, 2000; *Su*, 2004]. In winter there is a basin-wide cyclonic gyre, while in summer the circulation splits into a weakened cyclonic gyre north of about 12°N and a strong anticyclonic gyre south of it. These large scale circulations are established in a relatively short thermocline adjustment time of 1 to 4 months [*Liu et al.*, 2001]. Associated with these gyres are strong western boundary currents. In winter a southward jet flows along the entire western boundary [*Wyrtki*, 1961; *Liu et al.*, 2004]. In summer, there is a northward jet flowing along the western boundary in the southern SCS [*Xu et al.*, 1982]. The jet apparently veers eastward off central Vietnam near 12°N, which can be seen from many observations such as sea surface temperature and the chlorophyll signature [*Kuo et al.*, 2000; *Xie et al.*, 2003]. To the north, there is a narrow southwestern jet along the continental slope in the northwest SCS [*Qu*, 2000; *Metzger and Hurlburt*, 1996; *Su*, 2004]. In summary, a schematic diagram for the existing knowledge of the SCS circulation, modified after *Liu et al.* [2002], is shown in Figure 1. In their original diagram, the southwestward jet along the continental slope in the northwest SCS was not depicted for the summer.

[3] There is often a dipole structure associated with the summer eastward jet, with an anticyclonic eddy (AE) south of the jet and a cyclonic eddy (CE) north of it [e.g., *Shaw et al.*, 1999; *Wu et al.*, 1999; *Metzger and Hurlburt*, 1996; *Wang et al.*, 2003]. In fact, the eastward jet is rather conspicuous in the infrared satellite imageries because of the cold water from upwelling associated with the jet [*Kuo et al.*, 2000; *Xie et al.*, 2003]. Dynamic topography maps of *Fang et al.* [2002] and *Su et al.* [1999] indicate that the AE has a diameter of about 300 km and the eastward jet has a maximum velocity of around 0.8 ms^{-1}. Although numerical models by *Wu et al.* [1999] and *Metzger and Hurlburt* [1996] have produced this dipole structure, little is known about its generation mechanism. The present work focuses on the possible generation mechanism and the life cycle of the dipole structure.

2. Data

[4] Two satellite data sets, sea surface height anomaly (SSHA) and sea surface winds, are used to analyze the life cycle of the dipole. The SSHA data set is a multiple-altimeter product on a 1/8° × 1/8° grid covering the period of January 1993 to December 2000 from the US Naval Research Laboratory. It is derived from TOPEX/Poseidon (T/P), ERS and Geosat Follow On (GFO) altimetry, with the orbit error and tides removed, as discussed by *Jacobs et al.* [2002]. To avoid tidal aliasing from residual tidal effects, we apply a simple Hanning filter with a cut-off period around 60 days [*Wang et al.*, 2000]. The surface wind we use is a blended product from ERS1, ERS2, NSCAT and QuikSCAT data sets for the same period. The spatial resolutions of these four data sets are 1.0°, 1.0°, 0.5° and 0.25°, respectively. They are interpolated into a composite data set with a

[1] State Key Laboratory of Satellite Ocean Environment Dynamics, Second Institute of Oceanography, SOA, Hangzhou, China.
[2] Lamont-Doherty Earth Observatory, Columbia University, Palisades, New York, USA.

0148-0227/06/2005JC003314$09.00

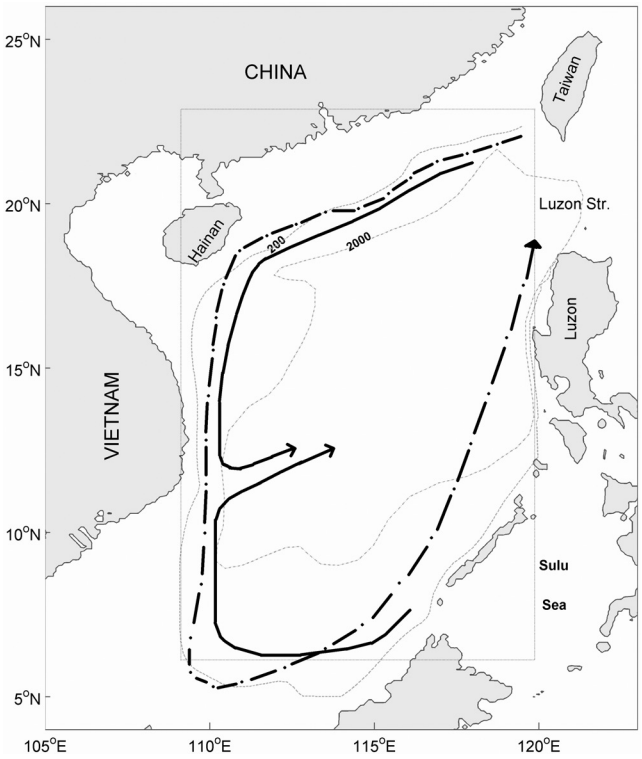

Figure 1. Map of the South China Sea. The two isobaths are for 200 m and 2000 m, respectively. The model SCS covers areas with water deeper than 200 m. The dotted rectangle represents the ideal rectangular basin used for simulations shown in Figures 5, 6 and 8. The schematic dashed streamline represents the basin-scale cyclonic gyre in winter, while the schematic solid streamlines represent, in summer, a basin-scale anticyclone gyre in the southern SCS and a cyclone gyre in the northern SCS (modified from *Liu et al.* [2002]).

spatial resolution of 0.25° and a temporal resolution of one week. The surface wind data is also used to force our numerical model to be discussed in section 4.

3. Methods

[5] We use a combination of observational data and model simulations for our analyses, with emphasis on the summer conditions. Based on the monsoonal nature of the SCS circulation, summer is defined in this study as the months from June to September. We also apply the Principal Component Analysis (PCA) [*Preisendorfer*, 1988] to examine the spatial pattern and the temporal variability of the SSHA and wind fields.

[6] The SSHA data from 1993 to 2000 show the appearance of the dipole structure each summer except for 1995 and 1998, when the cyclonic half of the dipole disappeared [*Wang*, 2004]. Strong warm events took place in the SCS in these two years, during which the SCS circulation was very different from other years, most likely due to changes in the wind field [*Shaw et al.*, 1999; *Xie et al.*, 2003]. To avoid data from the two warm events polluting the dipole signals of the other 6 normal years, all the mean fields in this study are obtained with the data from 1995 and 1998 excluded. For the PCA, however, we use all data from the 8 years between 1993 and 2000. Note that not every ENSO year results in a strong warm event in the SCS.

[7] A 1.5-layer reduced gravity model is applied to the SCS. Previous studies have shown the validity of such a model in simulating the SCS circulation [e.g., *Metzger and Hurlburt*, 1996]. The model equations are:

$$\frac{\partial U}{\partial t}+U\frac{\partial u}{\partial x}+V\frac{\partial u}{\partial y}+u\frac{\partial U}{\partial x}+v\frac{\partial U}{\partial y}-fV=-g'h\frac{\partial h}{\partial x}+A_h\left(\frac{\partial^2 U}{\partial x^2}+\frac{\partial^2 U}{\partial y^2}\right)-\nu\frac{\partial u}{\partial z}\bigg|_{z=h}+\nu\frac{\partial u}{\partial z}\bigg|_{z=0} \quad (1)$$

$$\frac{\partial V}{\partial t}+U\frac{\partial v}{\partial x}+V\frac{\partial v}{\partial y}+u\frac{\partial V}{\partial x}+v\frac{\partial V}{\partial y}+fU=-g'h\frac{\partial h}{\partial y}+A_h\left(\frac{\partial^2 V}{\partial x^2}+\frac{\partial^2 V}{\partial y^2}\right)-\nu\frac{\partial v}{\partial z}\bigg|_{z=h}+\nu\frac{\partial v}{\partial z}\bigg|_{z=0} \quad (2)$$

$$\frac{\partial h}{\partial t}+\frac{\partial U}{\partial x}+\frac{\partial V}{\partial y}=0 \quad (3)$$

where x, y and z are the conventional Cartesian coordinates, h the thermocline depth, u and v the components of velocity corresponding to x and y, respectively, U = hu and V = hv the total flows integrated over the entire water column from the thermocline to the surface, ρ the density, $g' = g\,\rho/\rho_0 = 0.03\ ms^{-2}$ the reduced gravity, ν the vertical diffusion coefficient and A_h the lateral friction coefficient. For the wind stress term, we let $\nu(\partial u/\partial z, \partial v/\partial z)|_{z=0} = Cd\ \rho_{air}\ U_w\ (u_w, v_w)$, where Cd is the drag coefficient, ρ_{air} the air density, U_w the wind speed and (u_w, v_w) the wind velocity. For the drag coefficient we take Cd = 0.0013 and the air density is 1.2 Kgm^{-3}. Except at the sea surface, we set the vertical friction to be zero. A_h is chosen so that stable statistics can be reached in long-term integration, facilitating analysis of the mesoscale eddies from the simulation results [*Hurlburt and Thompson*, 1980]. The grid Reynolds number, $Re = u\Delta x/A_h$, should also be greater than 10 [*Preller*, 1986]. In this study, through a series of sensitivity tests, we choose its value to be 500 m^2s^{-1}. Nonslip condition is applied at solid boundaries. As we shall explain in the following, all the boundaries of our model domain are solid boundaries. The model has been tested through simulating the classical problems addressed by *Veronis* [1966] and repeating the model results by *Hurlburt and Thompson* [1980]. The former is to test the nonlinear effect on a single gyre, while the latter is for eddy shedding. These tests give us confidence on the capability of the model in simulating mesoscale eddies.

[8] We choose the model SCS as the area in the SCS bordered by the 200 m isobath (Figure 1). The model grids are 0.25° × 0.25°. The grid size is shorter than the mean Munk width in the SCS, about 28 Km, satisfying the resolution requirement for western boundary currents in numerical simulation [*Berloff and McWilliams*, 1999]. It is also shorter than the climatological mean of the first baroclinic Rossby radius of deformation for the deep basin of the SCS, which is larger than 50 km [*Gan and Cai*, 2001]. To focus on the regional dynamics within the SCS in

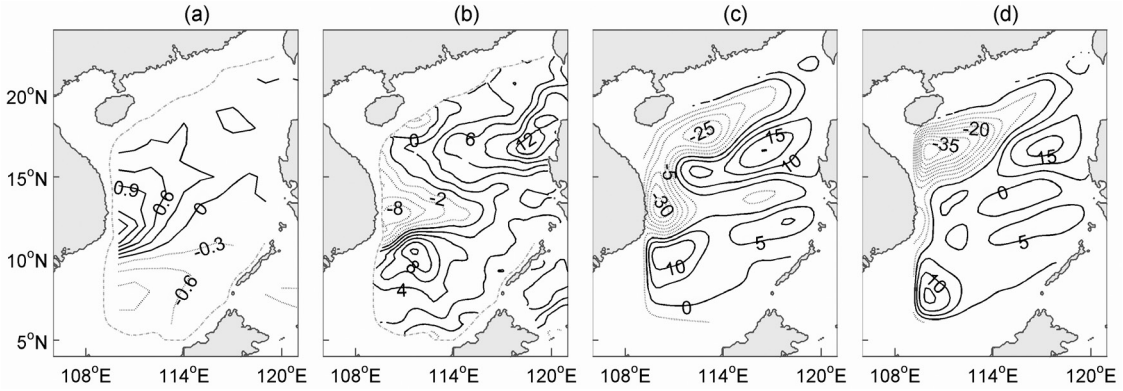

Figure 2. Satellite-data derived summertime mean fields, (a) WSC and (b) SSHA, during 1993–2000 (excluding the warm years of 1995 and 1998). Thermocline depth anomaly over the model SCS from (c) the nonlinear model and (d) the linearized model. Contour intervals in Figures 2a–2d are $0.3 \times \mathrm{N\,m^{-2}}$, 2 cm, 5 m and 5 m, respectively.

response to the winds, the only forcing imposed, we close the Luzon Strait. The initial thermocline depth is 200 m. The model is spun up with the winds switched on gradually from zero to that of January 1993 over a period of 1 month. Then the model is forced with 1993 wind repeated for four years to allow the upper ocean circulation to reach a quasi-steady state. Finally, the model is forced with the winds from January 1993 to December 2000. However, the mean simulated fields are computed without using the results from 1995 and 1998, for the reason mentioned above.

4. Results

4.1. Observations

[9] The satellite-data derived mean summer wind stress curl (WSC) is positive (negative) in the northwestern (southeastern) SCS (Figure 2a), as was demonstrated in past studies [e.g., *Qu*, 2000]. The WCS pattern is associated with the southwest summer wind jet off the central Vietnam, which is in fact a result of the orographic effects on the summer monsoon from the Annam Cordillera mountain range [*Xie et al.*, 2003]. The mean summer SSHA field derived from altimetry satellite (Figure 2b) reflects the WSC pattern, with a cyclonic gyre north of about 12°N and an anticyclonic gyre south of it. There is also a sub-basin anticyclonic gyre off northwestern Luzon, likely reflecting the anticyclonic eddy generated there yearly during the summer between 1993 and 2000 [*Wang*, 2004]. The dipole structure of AE-CE eddy pair off central Vietnam is also clearly evident in Figure 2b.

[10] The southwest monsoon establishes rapidly over the SCS in June, reaches peak in July to August, slackens off in September, and finally is replaced by the northeast monsoon in October [*Liang*, 1991]. Figures 3a and 3b show, respectively, the satellite-data derived monthly mean WSC and SSHA from June to October. The WSC has a cyclonic (anticyclonic) pattern in the northwest (southwest) SCS during the summer months, but such a pattern disappears in October. The dipole structure begins to take its form in June with the AE to the south and the CE to the north. The dipole intensifies as summer progresses, along with the development of the eastward jet between the two eddies. Both the AE and CE are the strongest in September, with the eddy center's SSHA reaching 17 cm and −16 cm, respectively. In October the AE is much weakened and dissipates out.

[11] We use the PCA to investigate the relation between the WSC field and the dipole identified from the SSHA field, both based on satellite data. To focus on the signal of the dipole structure, we only use the data from the area of 110–116°E, 6–10°N for the PCA. Since circulation in the SCS is driven primarily by the monsoon, there are only two dominant modes, the summer and winter modes, respectively, for either WSC or SSHA. Here we only analyze the summer modes of the two fields. The summer mode for the WSC field (Figure 4a) is positive (negative) north (south) of about 10°N and accounts for 57% of the total WSC variance. The summer mode for the SSHA (Figure 4b) shows a clear dipole structure and accounts for 28% of the total SSHA variance. The two time series of the normalized expansion coefficients for the two summer modes (Figure 4c) show a good correlation in every summer except for 1995 and 1998. Furthermore, there is a time lag between the dipole and the WSC. The lag-correlation for the two time series (Figure 4d) suggests that the dipole usually lags behind WSC by about 40 days. This is roughly the time for the first baroclinic wave to propagate across the southern basin of the SCS, indicating that the dipole structure is strongly associated with the SCS basin scale circulation.

4.2. Dynamics of the Dipole Structure

[12] It is well known that nonlinearity is important for the generation of mesoscale eddies in the large-scale wind-driven ocean circulation [*Bryan*, 1963; *Veronis*, 1966]. *Liu et al.* [2001] has shown that the dynamics of the basin-wide circulation in the SCS is similar to the wind-driven general circulation and that a reduced gravity model can be used to understand its basic dynamics. Therefore, it should be instructive to look at the generation of the summer dipole structure off central Vietnam with a reduced gravity model.

[13] Figures 2c and 2d show the modeled mean summer circulation anomaly over the model SCS from 1993 to 2000 (excluding 1995 and 1998) from our reduced-gravity model and its linearized version, respectively, both driven by the wind field derived from satellite-data. The dipole structure and the accompanying eastward current between the two

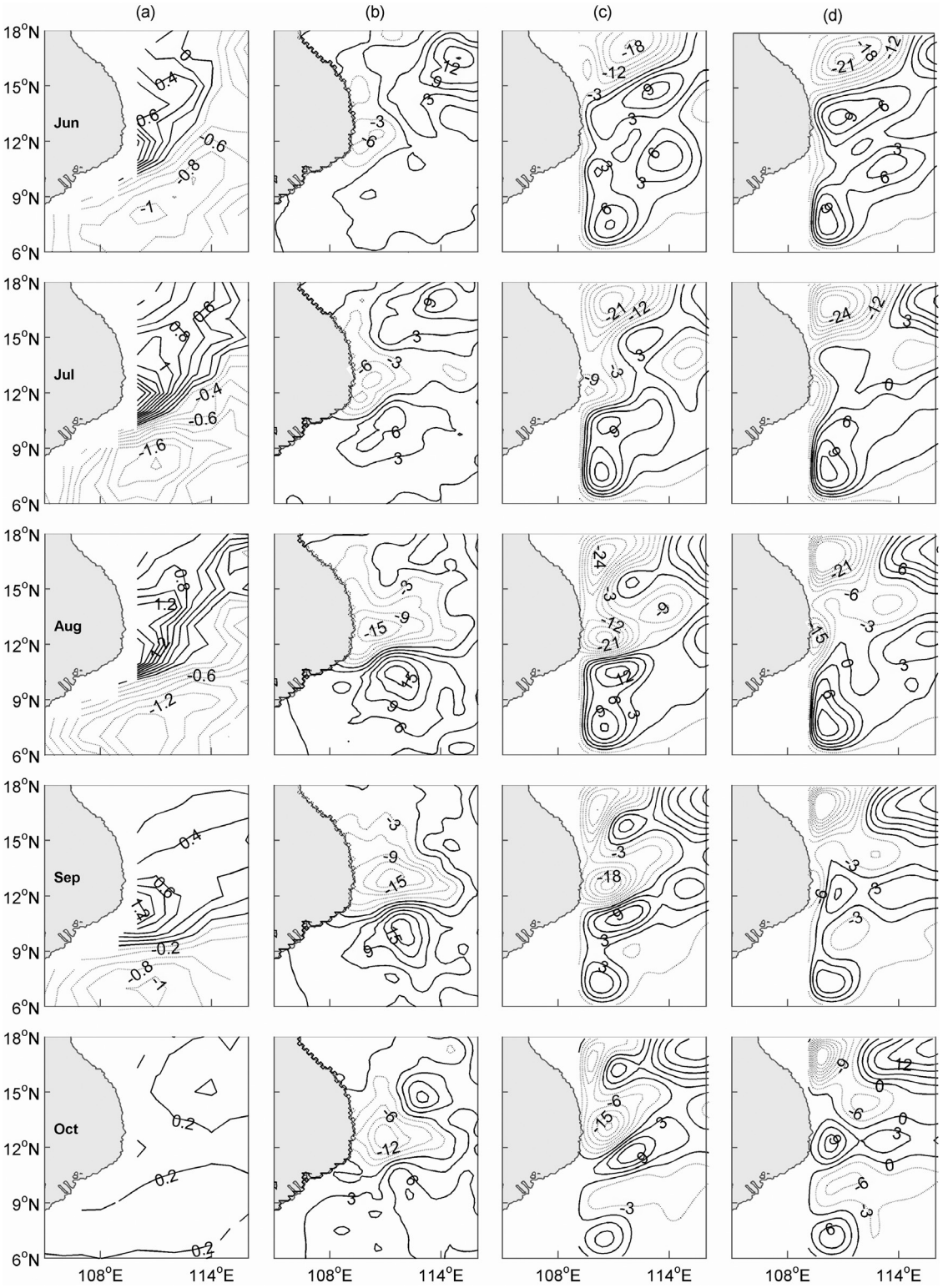

Figure 3. Monthly mean maps of (a) WSC and (b) SSHA derived from satellite data during 1993–2000 (excluding warm years of 1995 and 1998). Thermocline depth anomaly over the model SCS from (c) the nonlinear model and (d) the linear model. Contour intervals in Figures 3a–3d are 0.2 N m^{-2}, 3 cm, 3 m and 3 m, respectively.

eddies are clearly evident from the results of the nonlinear system. Both systems generate a mean cyclonic (anticyclonic) gyre in the northern (southern) SCS. The northern gyre has a southward western boundary current, in agreement with observations [*Qu*, 2000, Figure 2b] and previous modeling studies [*Metzger and Hurlburt*, 1996]. Offshore of this southward western boundary current there is a northward current, also in agreement with the observations and

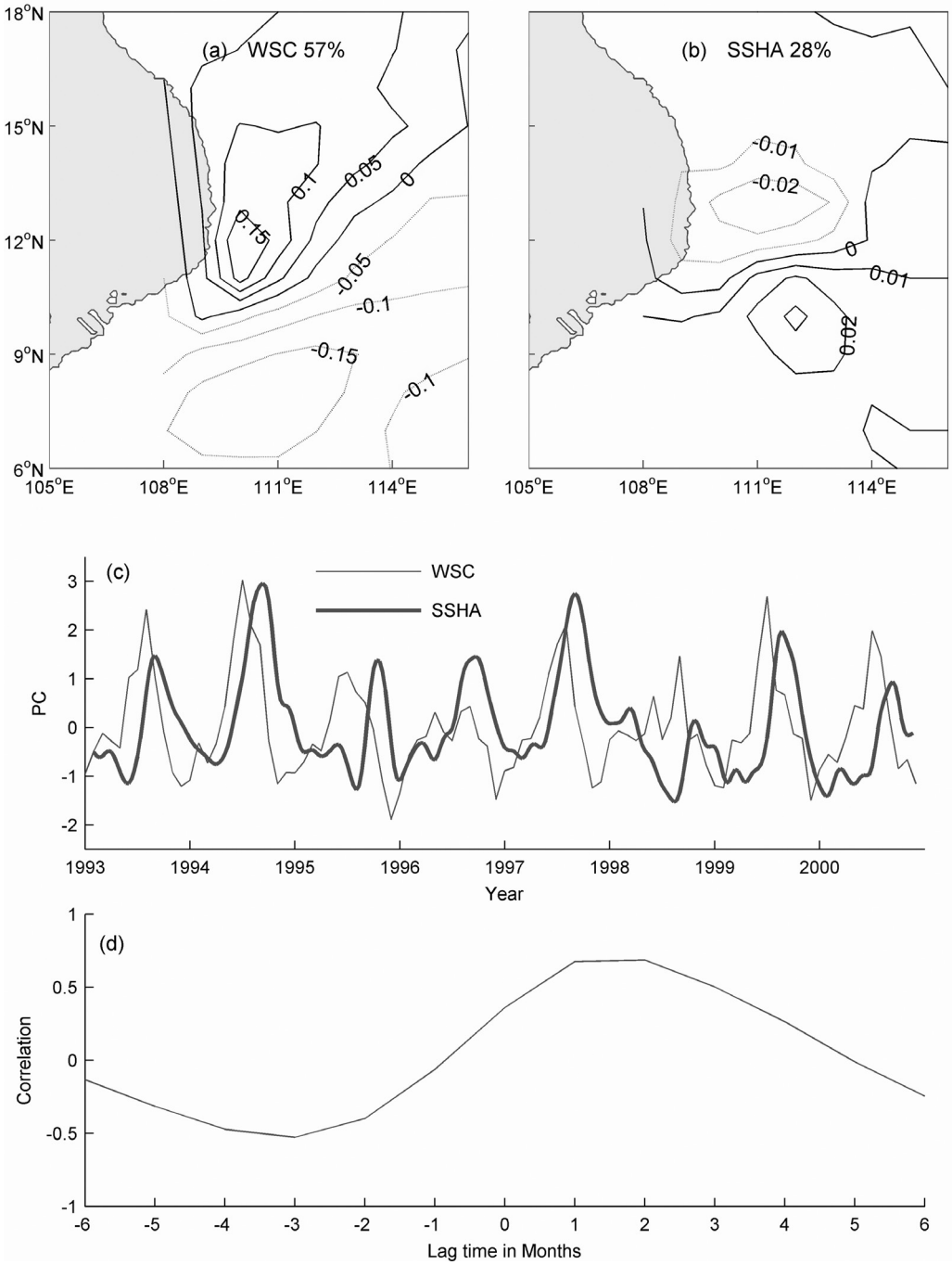

Figure 4. Normalized summer modes of (a) WSC and (b) SSHA, based on satellite data from 1993 to 2000. (c) Time series of the expansion coefficients (principal components, PC) of Figures 4a and 4b, normalized by the standard deviation of the respective original PC. (d) Lag correlation between SSHA and WSC.

modeling results mentioned above. In the linearized system, however, the dipole and the eastward jet off central Vietnam are not present. Comparing the two simulated mean dipole structures (jet width, jet length and the strength of the two eddies) with the mean SSHA observation derived from satellite data, it is evident that the nonlinear model simulation is much more realistic than the linearized one.

[14] To further examine the effects of nonlinearity, we show the life cycle of the dipole structure off central Vietnam from the reduced-gravity model and its linearized version, respectively, both driven by the wind field derived from the satellite-data. For the nonlinear system (Figure 3c), both the eastward jet and the strength of the dipole are weak in June, intensify in July, and reach their peaks in August and September. In October, the AE of the dipole is dissipating out. These simulations resemble the satellite data derived SSHA observations of the life cycle of the dipole (Figure 3b). As to the linear system (Figure 3d), from June through October the eastward jet and the dipole are never fully developed. We conclude that nonlinearity is very

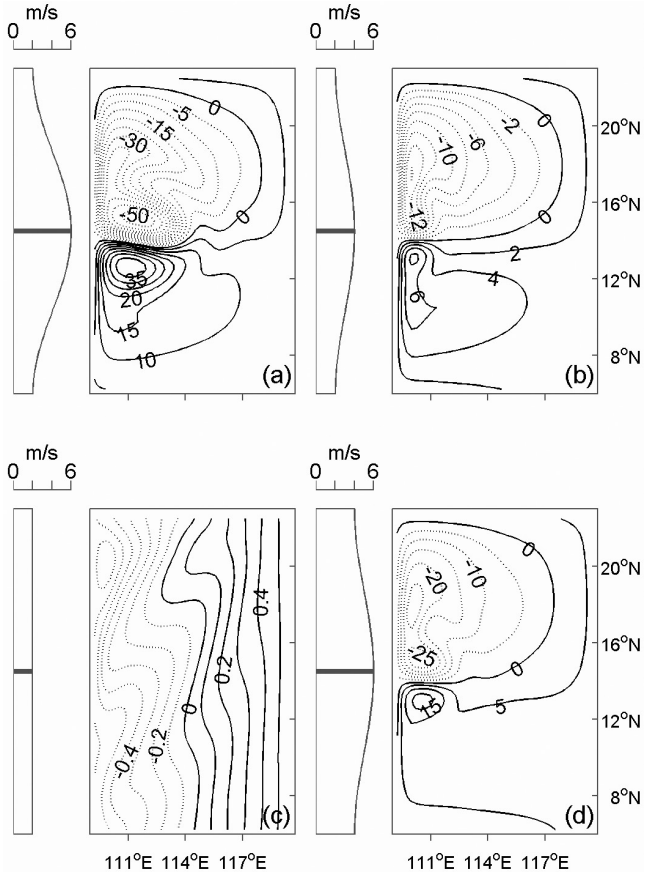

Figure 5. Dipole structure in the ideal rectangular basin driven by a westerly wind jet. The zonal wind speed is set at a constant value of 2 ms^{-1} at the northern/southern boundary and at, respectively, (a) 6 ms^{-1}, (b) 4 ms^{-1}, and (c) 2 ms^{-1} at the midbasin (14.75°N). (d) The zonal wind speed is set at 6 ms^{-1} at the midbasin and at 4 ms^{-1} at the northern/southern boundary. The wind speed in between the end boundaries varies as a cosine function.

important to the dipole dynamics. We note that there is a small but prominent anticyclonic core at the southwestern corner of the model domain in the simulated thermocline depth anomaly (Figures 3c and 3d), which is not found in the observation (Figure 3b). The model result is actually a reflection of the cyclonic eddy there in winter, a dominant feature in the simulation [*Wang*, 2004; also see *Metzger and Hurlburt*, 1996]. Both field [*Fang et al.*, 2002] and SSHA observations in winter, however, show only a weak cyclonic eddy appearing, sometimes, around that general area. Deficiency of our model, (such as lack of bathymetry and reduced domain with closed boundaries at the southwestern corner) is likely the reason for this discrepancy.

[15] *Veronis* [1966] has analyzed the effect of nonlinear terms on the wind-driven general circulation in the Atlantic Ocean. His findings can be used to explain the dipole structure of the SCS as following: In the southern SCS, the net effect of inertial process of the wind-driven southern gyre is to advect negative vorticity northward by its northward western boundary current, concentrating negative vorticity into the northwest corner of the southern gyre to form AE. While in the northern SCS, the net effect of inertial process of the wind-driven northern gyre is to advect positive vorticity southward by its southward western boundary current, concentrating positive vorticity into the southwest corner of the northern gyre to form CE. Such vorticity transports from the two western boundary currents result in the dipole structure off central Vietnam, with an eastward current jet in between. It is interesting to note that this pair of eddies are elongated toward the east, with the jet extending quite far offshore. This is obviously caused by the inertial effect of the jet itself.

4.3. Wind Field and the Dipole Structure

[16] The above results from the reduced gravity model over the model SCS indicate that the dipole seems to be a result of two opposite wind-driven gyres. Thus the wind field should be important to the dipole formation. To see how the wind field affects the dipole structure, we apply our model to, for clarity, an ideal rectangular basin under ideal wind forcing. The basin has a scale of 1000 km × 1700 km spanning from 6°N to 23°N (Figure 1), resembling the SCS. As the southwest summer wind jet off the central Vietnam has significant variablity [*Xie et al.*, 2003], we will focus on the effects of the wind structure, such as the strength of the wind jet, asymmetry of the zonal wind field and direction of the wind jet, on the dipole structure. Comparatively speaking, the width of the jet is not as important to the dipole structure (figures omitted). For experiments with the ideal rectangular basin, each of them is spun up from rest until reaching statistical equilibrium, as determined by its corresponding total kinetic energy level of the entire basin. The concerned variables are then averaged over the next 180 days, and these results are used for analysis. The statistical reliability of such time averages has been discussed by *Holland and Rhines* [1980].

[17] To examine the effects of the wind-jet strength on the dipole, we consider a symmetric westerly zonal wind jet with a cosine meridional variation (Figure 5). Its strength at both the southern and northern ends is set at a constant 2 ms^{-1}. Three experiments, with the wind jet strength at the middle of the basin (around 14.75°N) set at 6, 4 and 2 ms^{-1}, respectively, are carried out. The dipole structure weakens with the decrease in the wind-jet strength (Figures 5a and 5b). The weaker the wind jet (weaker wind stress curl field), the nearer the dipole is to the Vietnam coast and the weaker are the accompanying jet and eddies. As expected, without the wind stress curls, the two recirculation gyres will not develop, and hence, in the absence of western boundary currents transporting opposite vorticity to the region off central Vietnam, the dipole structure cannot form (Figure 5c).

[18] As discussed in section 4.2, nonlinearity is quite important to the dipole dynamics. Thus the overall strength of the winds may have significant influence on the dipole structure. In Figure 5d we add a uniform westerly wind of 2 ms^{-1} to the wind profile of Figure 5b. As expected, the enhanced wind field results in a much stronger dipole with its two cores further offshore (Figures 5b and 5d), though the wind stress curls are the same for both experiments. However, compared to the nonlinearity effects, the input of vorticity from the wind stress curl is equally, if not more, important to the dipole structure (Figures 5a and 5d).

[19] To investigate the effects of the asymmetry of a zonal wind field on the dipole, two experiments are conducted.

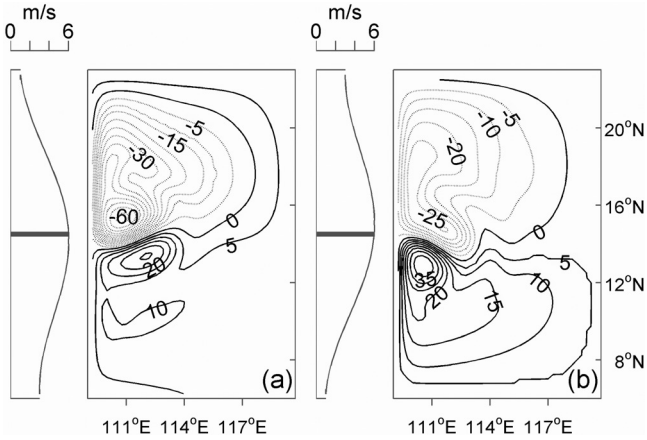

Figure 6. Dipole structure in an ideal rectangular basin driven by an asymmetric westerly wind jet. The zonal wind speed distribution is the sum of three components, namely, a constant, a linear shear and a cosine function. The wind speed at the midbasin (14.75°N) is set at a constant value of 6 ms^{-1} and varies as (a) $4 + 2 \times \cos(\pi y/850) - y/850$ and (b) $4 + 2 \times \cos(\pi y/850) + y/850$, where y is the distance (km) from the zero at the midbasin. Note that the maximum wind speed is slightly off the midbasin position, at $(850/\pi) \times \text{Arcsin}(1/2\pi)$ km south of the midbasin for Figure 6a and north of the midbasin for Figure 6b.

The zonal wind speed distribution is chosen to be the sum of three components, namely, a constant, a linear shear and a cosine function, namely, as $3 + (1 - y/850) + 2 \times \cos(\pi y/850)$ and $3 + (1 + y/850) + 2 \times \cos(\pi y/850)$, respectively, for the two experiments (Figures 6a and 6b), where y is the distance (km) from the zero at the midbasin. The maximum wind speed is slightly off the midbasin position, i.e., at $(850/\pi) \times \text{Arcsin}(1/2\pi)$ km south of the midbasin for Figure 6a and north of the midbasin for Figure 6b. Approximately speaking, such a wind speed distribution is like imposing a constant positive (or negative) wind stress curl to the one used in Figure 5a. Compared with the symmetric wind field case (Figure 5a), the experiment in Figure 6a shows a strengthened CE, a weakened AE and an east-northeastward ocean jet, whereas the experiment in Figure 6b shows a weakened CE, a strengthened AE and a southeastward ocean jet. It is known that, for a wind field with a constant positive (or negative) wind stress curl, the resulting circulation is a single basin-wide cyclonic (or anticyclonic) gyre with energetic currents at its southwest (northwest) part because of the inertia effects. The changing strength of the eddies in Figures 6a and 6b can thus be understood. Furthermore, the position of eddies are influenced by planetary and nonlinear self advective propagation tendencies. For Figure 6a, stronger cyclonic gyre over the north basin results in stronger southward western boundary current, thus the southward advective propagation tendency of the CE is strengthened and the inertial southward western boundary current overshoots the maximum wind stress line (at middle basin). Furthermore, the nonlinear process also causes the appearance of a tighter cyclonic eddy, which leads to the separation moving to the north of the middle basin line and the northeastward jet wrapping around the stronger cyclonic eddy [*Jiang et al.*, 1995]. The opposite is true for the circulation in Figure 6b.

[20] Circulations in the model SCS forced by the summer-mean wind data and only its zonal component are shown, respectively, in Figures 7a and 7b. The two circulation patterns are similar. However, compared to the true wind field case, the zonal wind component forced circulation show a weaker CE and a more eastward ocean jet situated slightly further to the south. For the case with only the meridional winds imposed, there is no dipole structure formed (figure not shown). These suggest that, for the SCS, the zonal winds are essential to the formation of the dipole, but the meridional winds also play an important role in the dipole strength and the position/orientation of the ocean jet off central Vietnam.

[21] To further study the effects of the meridional component of the wind jet on the dipole structure, we carry out 3 experiments with a southerly wind jet orienting at an angle of 10°, 20° and 30°, respectively, counterclockwise from the east (Figure 8). The wind jet velocity along the middle basin is again set at 6 ms^{-1}, as in Figure 5a, for all three experiments. Both the directions and the middle basin wind-jet strength are chosen as the representative ones, based on the monthly means of the eight years wind data. Compared with the westerly winds case (Figure 5), the southwesterly winds cause the CE positioning closer to the western boundary of the basin and the AE extending further offshore (Figure 8), similar to the SSHA pattern from the observation (Figure 3b). The greater the inclination of the winds, the further the CE (AE) is pushed westward (eastward). The orientation of the wind jet changes the vorticity input to the southern and northern gyre, thus altering the dipole strength and the relative position of the two concomitant eddies through changing the strength of the western boundary currents associated with the two gyres. However, how the wind jet itself drives the eastward ocean jet is not clear.

[22] The above experiments show that, through nonlinear processes, the strength and location of the recirculation gyres are sensitive to the input of vorticity, wind strength and wind direction. Such conclusion has been reached by many previous studies, using both quasigeostrophic barotropic models [e.g., *Cessi and Ierley*, 1995; *Jayne and*

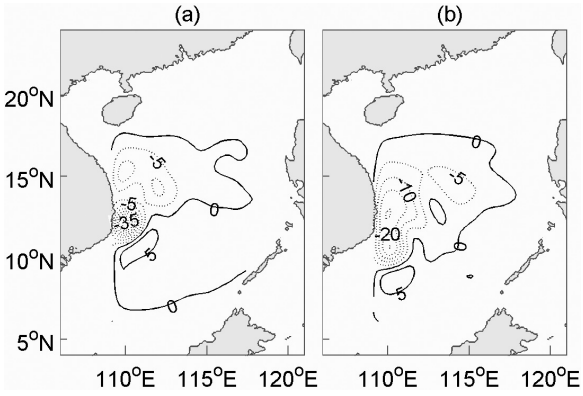

Figure 7. Dipole structure in SCS basin driven by summer mean wind field derived from satellite data. (a) Both zonal wind and meridional wind; (b) only zonal wind.

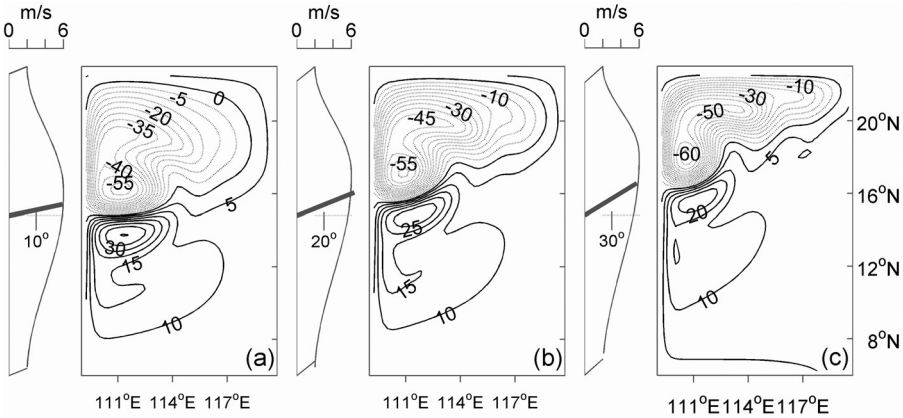

Figure 8. Dipole structure in an idealized model basin driven by a southwesterly wind jet. The wind speed is 2 ms^{-1} at the northern/southern boundary, 6 ms^{-1} in the middle basin, and varies as a cosine function in between. The direction of the southwest wind jet is (a) 10°, (b) 20° and (c) 30° counterclockwise from the east. The wind jet's meridional part is equal to zonal part multiplied by a tangent function of the direction.

Hogg, 1999; *Fox-Kemper and Pedlosky*, 2004] and reduced gravity shallow models [e.g., *Jiang et al.*, 1995; *Simonnet et al.*, 2003]. Furthermore, they have also demonstrated that the strength and location of the recirculation gyres are very sensitive to other details such as the Reynolds number of the flow, bottom drag, numerical discretization, stratification, entrainment etc. However, many issues warrant further study. For example, our circulation pattern in Figure 5a, including its inertia and Munk boundary layer parameters, is similar to case N2, an unstable circulation, of *Cessi and Ierley* [1995], who uses a quasigeostrophic barotropic model. On the other hand, results from the reduced gravity model by *Simonnet et al.* [2003] show a similar but stable circulation. Other factors can also influence the eddy dynamics. For example, entrainment of water from deeper layer may cool the sea surface temperature offshore and then virtually eliminates the cyclonic eddy [*McCreary et al.*, 1989]. Thus, for the SCS, many details of the dipole and their relative strength and location must be further explored in a three-dimensional high-resolution model. Nevertheless, the fundamental dynamics of the summer dipole in the SCS shown here are basically correct.

5. Summary and Discussion

[23] Based on the results shown above, we can describe the dynamics of the summer dipole structure off central Vietnam as follows. As the summer monsoon wind impinges on the Annam Cordillera, a strong southwest wind jet appears, with positive (negative) WSC in the northern (southern) SCS. The WSC field drives two basin-scale gyres in the SCS, a cyclonic one north of about 12°N and an anticyclonic one south of it. Associated with these gyres are a southward boundary current along the northwestern boundary and a northward one along the southwestern boundary. The vorticity transport through the inertial process by these currents results in the formation of the AE (CE) off the central Vietnam in summer. An eastward jet is formed between the AE and CE, and is extended further offshore by the inertia of the jet itself.

[24] Both the SSHA observations and the numerical simulations show that the dipole structure begins in June, peaks in August and September, and dissipates out in October. The SSHA field lags behind the wind field by about 40 days, which corresponds to the basin-crossing time of the baroclinic Rossby waves near 12°N. The reason is that, when the wind field changes, the gyre circulation and thus the western boundary currents will respond accordingly with a Rossby adjustment time of approximately 40 days. The dipole, being associated with vorticity transport by the western boundary currents, also fluctuates with the wind field at a 40-day lag.

[25] Our numerical results show that the strength of the wind stress curl is responsible for the generation and maintenance of the dipole structure. The strength and relative positions of the two concomitant eddies are sensitive to the direction of the wind jet and zonal wind fields' asymmetry.

[26] There are four possible deficiencies associated with our model settings that may account for the differences between simulated and observed dipole structure. Firstly, we defined the 200 m isobaths as a solid wall boundary, which will result in western boundary currents stronger than what are present in the SCS. Secondly, we have closed the Luzon Strait, which cuts off the strong influence from the Kuroshio [*Liu et al.*, 2001]. Thirdly, we have also closed the strait between the SCS and the Sulu Sea, which may underestimate the strength of the eastward current as there is likely a significant outflow through the Sulu Sea [*Su*, 2004]. Finally, lack of entrainment mechanism in our model may affect the dipole structure because of the accompanying strong upwelling off Vietnam in summer. Since the fundamental dynamics of the summer dipole in the SCS is shown to be wind-driven and nonlinear, further understanding of its dynamics needs high-resolution three-dimensional models.

[27] **Acknowledgments.** The study was supported by NSFC (grants 40576019 and 40576012) and the Major State Basic Research Program of China (grant G1999043805). We wish to thank Yu Zuojun for helpful discussions and constructive suggestions on the paper. Suggestions by the two anonymous reviewers have greatly improved this paper.

References

Berloff, P., and J. McWilliams (1999), Large-scale low-frequency variability in wind-driven ocean gyres, *J. Phys. Oceanogr.*, *29*, 1925–1949.

Bryan, K. (1963), A numerical investigation of a nonlinear model of a wind-driven ocean, *J. Atmos. Sci.*, *20*, 594–606.

Cessi, P., and G. R. Ierley (1995), Symmetry-breaking multiple equilibria in quasigeostrophic, wind-driven flows, *J. Phys. Oceanogr.*, *25*, 1196–1205.

Fang, W. D., G. H. Fang, P. Shi, Q. Z. Huang, and Q. Xie (2002), Seasonal structures of upper layer circulation in the southern South China Sea from in situ observations, *J. Geophys. Res.*, *107*(C11), 3202, doi:10.1029/2002JC001343.

Fox-Kemper, B., and J. Pedlosky (2004), Wind-driven barotropic gyre I: Circulation control by eddy vorticity fluxes to an enhanced removal region, *J. Mar. Res.*, *62*, 169–193.

Gan, Z. J., and S. Q. Cai (2001), Geographical and seasonal variability of Rossby Radii in South China Sea, *J. Trop. Oceanogr.*, *20*(1), 1–9.

Holland, W. R., and P. B. Rhines (1980), An example of eddy induced ocean circulation, *J. Phys. Oceanogr.*, *10*, 1010–1031.

Hurlburt, H. E., and J. D. Thompson (1980), A numerical study of Loop Current intrusions and eddy shedding, *J. Phys. Oceanogr.*, *10*, 1611–1651.

Jacobs, G. A., C. N. Barron, D. N. Fox, K. R. Whimer, S. Klingenberger, D. May, and J. P. Blaha (2002), Operational altimeter sea level products, *Oceanography*, *15*, 13–21.

Jayne, S. R., and N. G. Hogg (1999), On recirculation forced by an unstable jet, *J. Phys. Oceanogr.*, *29*, 2711–2718.

Jiang, S., F.-F. Jin, and M. Ghil (1995), Multiple-equilibria, periodic and aperiodic solutions in a wind-driven, double-gyre shallow-water model, *J. Phys. Oceanogr.*, *25*, 764–786.

Kuo, N. J., Q. A. Zheng, and C. R. Ho (2000), Satellite observation of upwelling along the western coast of the South China Sea, *Remote Sens. Environ.*, *74*, 463–470.

Liang, B. Q. (1991), *Tropical Atmospheric Circulation System Over the South China Sea (in Chinese)*, 224 pp., China Meteorol. Press, Beijing.

Liu, K.-K., S.-Y. Chao, P.-T. Shaw, G. C. Gong, C. C. Chen, and T. Y. Tang (2002), Monsoon forced chlorophyll distribution and primary productivity in the South China Sea: Observations and a numerical study, *Deep Sea Res., Part I*, *49*, 1387–1412.

Liu, Q. Y., X. Jiang, S. P. Xie, and W. T. Liu (2004), A gap in the Indo-Pacific warm pool over the South China Sea in boreal winter: Seasonal development and interannual variability, *J. Geophys. Res.*, *109*, C07012, doi:10.1029/2003JC002179.

Liu, Z. Y., H. J. Yang, and Q. Y. Liu (2001), Regional dynamics of seasonal variability in the South China Sea, *J. Phys. Oceanogr.*, *31*, 272–284.

McCreary, J. P., H. S. Lee, and D. B. Enfield (1989), The response of the coastal ocean to strong offshore winds: With application to circulations in the Gulfs of Tehuantepec and Papagayo, *J. Mar. Res.*, *47*, 81–109.

Metzger, E. J., and H. Hurlburt (1996), Coupled dynamics of the South China Sea, the Sulu Sea, and the Pacific Ocean, *J. Geophys. Res.*, *101*, 12,331–12,352.

Preisendorfer, R. W. (1988), *Principal Component Analysis in Meteorology and Oceanography*, 425 pp., Elsevier, New York.

Preller, R. H. (1986), A numerical model study of Alboran Sea Gyre, *Prog. Oceanogr.*, *16*, 113–146.

Qu, T. D. (2000), Upper-layer circulation in the South China Sea, *J. Phys. Oceanogr.*, *30*, 1450–1460.

Shaw, P. T., S. Y. Chao, and L. L. Fu (1999), Sea surface height variation in the South China Sea from satellite altimetry, *Oceanol. ACTA*, *22*, 1–17.

Simonnet, E., M. Ghil, K. Ide, R. Temam, and S. Wang (2003), Low-frequency variability in shallow-water models of the wind-driven ocean circulation, *J. Phys. Oceanogr.*, *33*, 712–752.

Su, J. (2004), Overview of the South China Sea circulation and its influence on the coastal physical oceanography near the Pearl River Estuary, *Cont. Shelf Res.*, *24*, 1745–1760.

Su, J., J. P. Xu, S. Q. Cai, and O. Wang (1999), Gyres and eddies in the South China Sea, in *Onset and Evolution of the South China Sea Monsoon and Its Interaction With the Ocean*, edited by Y. Ding and C. Li, pp. 272–279, China Meteorol. Press, Beijing.

Veronis, G. (1966), Wind-driven ocean circulation—part 2: Numerical solutions of the nonlinear problem, *Deep Sea Res.*, *13*, 17–29.

Wang, G. H. (2004), Discussion on the movement of mesoscale eddies in the South China Sea (in Chinese), Ph.D. dissertation, Sch. of Phys. Oceanogr., Ocean Univ. of China, Qingdao, China.

Wang, G. H., J. Su, and P. C. Chu (2003), Mesoscale eddies in the South China Sea detected from altimeter data, *Geophys. Res. Lett.*, *30*(21), 2121, doi:10.1029/2003GL018532.

Wang, L. P., C. J. Koblinsky, and S. Howden (2000), Mesoscale variability in the South China Sea from the TOPEX/Poseidon altimetry data, *Deep Sea Res., Part I*, *47*, 681–708.

Wu, C. R., P. T. Shaw, and S. Y. Chao (1999), Assimilating altimetric data into a South China Sea model, *J. Geophys. Res.*, *104*, 29,987–30,005.

Wyrtki, K. (1961), Scientific results of marine investigation of the South China Sea and Gulf of Thailand, *NAGA Rep., 2*, 195 pp.

Xie, S. P., Q. Xie, D. X. Wang, and W. T. Liu (2003), Summer upwelling in the South China Sea and its role in regional climate variations, *J. Geophys. Res.*, *108*(C8), 3261, doi:10.1029/2003JC001867.

Xu, X. Z., Z. Qiu, and H. C. Chen (1982), The general descriptions of the horizontal circulation in the South China Sea, in *Proceedings of the 1980 Symposium on Hydrometeorology* (in Chinese), pp. 137–145, Chin. Soc. of Oceanol. and Limnol., Sci. Press, Beijing.

D. Chen, Lamont-Doherty Earth Observatory, Columbia University, Palisades, NY 10964-1000, USA.

J. Su and G. Wang, State Key Laboratory of Satellite Ocean Environment Dynamics, Second Institute of Oceanography, SOA, 310012 Hangzhou, China. (guihua_wanggh@yahoo.com.cn)